

Observation of magnetic skyrmion crystals in a van der Waals ferromagnet Fe₃GeTe₂

Authors: Tae-Eon Park,¹ Licong Peng,² Xichao Zhang,³ Sung Jong Kim,^{1,4} Kyung Mee Song,¹ Kwangsu Kim,^{1,5} Markus Weigand,⁶ Gisela Schütz,⁷ Simone Finizio,⁸ Jörg Raabe,⁸ Jing Xia,³ Yan Zhou,³ Motohiko Ezawa,⁹ Xiaoxi Liu,¹⁰ Joonyeon Chang,^{1,11} Hyun Cheol Koo,^{1,4} Young Duck Kim,¹² Xiuzhen Yu,² Seonghoon Woo^{13*}

Affiliations:

¹Center for Spintronics, Korea Institute of Science and Technology, Seoul 02792, Korea

²RIKEN Center for Emergent Matter Science, Wako, 351-0198, Japan

³School of Science and Engineering, The Chinese University of Hong Kong, Shenzhen, Guangdong 518172, China

⁴KU-KIST Graduate School of Converging Science and Technology, Korea University, Seoul 02841, Korea

⁵Department of Physics, University of Ulsan, Ulsan 44610, Korea

⁶Helmholtz-Center Berlin, Albert-Einstein-Straße 15, 12489 Berlin, Germany

⁷Max-Planck-Institut für Intelligente Systeme, 70569 Stuttgart, Germany

⁸Swiss Light Source, Paul Scherrer Institut, 5232 Villigen, Switzerland

⁹Department of Applied Physics, University of Tokyo, Hongo 7-3-1, Tokyo 113-8656, Japan

¹⁰Department of Electrical and Computer Engineering, Shinshu University, Wakasato 4-17-1, Nagano 380-8553, Japan

¹¹Department of Materials Science & Engineering, Yonsei University, Seoul 03722, Korea

¹²Department of Physics, Kyung Hee University, Seoul 02447, Korea

¹³IBM T.J. Watson Research Center, 1101 Kitchawan Rd, Yorktown Heights, New York 10598, USA

* Author to whom correspondence should be addressed: shwoo@ibm.com

Since the discovery of long-range magnetic orders in the two-dimensional (2D) van der Waals (vdW) crystals,^{1,2} significant interest on such 2D magnets has emerged, inspired by their appealing physical properties and integration with other 2D family for unique heterostructures¹⁻⁸. In known 2D magnets such as $\text{Cr}_2\text{Ge}_2\text{Te}_6$ ¹, CrI_3 ²⁻⁴ and Fe_3GeTe_2 ⁵, spin-orbit coupling (SOC) stabilizes perpendicular magnetic anisotropy (PMA) down to one or few monolayers. Such a strong SOC could also lift the chiral degeneracy, leading to the formation of topological magnetic configurations such as skyrmions^{9,10} through the Dzyaloshinskii-Moriya interaction (DMI)^{11,12}. Here, we report the experimental observation of magnetic skyrmions and their ordered crystal structures in a vdW ferromagnet Fe_3GeTe_2 . Using high-resolution scanning transmission X-ray microscopy (STXM) and Lorentz transmission electron microscopy (LTEM) measurements, we demonstrate that a skyrmion crystal (SkX) state in Fe_3GeTe_2 can be generated by both dynamically using current pulses and statically using canted magnetic fields, where our LTEM measurements suggest that the observed skyrmions in SkX state are homochiral. Our finding opens the door to chiral magnetism and topological spin textures based on 2D vdW magnets, which will pave a new avenue towards 2D magnet-based topological spintronics.

Two-dimensional (2D) van der Waals (vdW) crystals have been significantly highlighted as a unique material platform, mainly due to their fascinating physical properties, low-cost fabrication and high integrability to produce appealing artificial heterostructures^{13,14}. Recent addition of magnetic 2D vdW crystals, where intrinsic long-range magnetic orders were observed in $\text{Cr}_2\text{Ge}_2\text{Te}_6$ (ref.¹) and CrI_3 (ref.²), offered a new building block to this platform, opening a whole new door to vdW magnet-based spintronics^{6–8}. Therefore, significant following interests have emerged and rapidly demonstrated few key elements for applications, including the magnetoresistance (MR) effects^{3,4} and gate-tunable room-temperature magnetism⁵.

Whereas the long-range magnetic order is often suppressed in vdW crystals due to thermal fluctuations given by Mermin-Wagner theorem,¹⁵ strong spin-orbit coupling (SOC) in vdW magnets plays an essential role in stabilizing the perpendicular magnetic anisotropy (PMA) and thus overcomes the thermal fluctuations down to a monolayer limit.^{2,5} In a material with such large SOC and broken inversion symmetry, the anti-symmetric exchange interaction, so called Dzyaloshinskii-Moriya interaction (DMI)^{11,12}, can emerge and strong enough to stabilize topological magnetic configurations including skyrmions^{9,10}. Recent theoretical works have also discussed the emergence of DMI in 2D vdW magnets with various possible origins, e.g. crystal symmetry or sample boundary, as well as resulting skyrmion stabilization^{16–18}. However, experimental demonstration of chiral magnetic configurations or skyrmions in such vdW magnets has remained elusive and challenging.

Here we present the observation of magnetic skyrmions and their ordered crystal structures in a vdW ferromagnetic Fe_3GeTe_2 (FGT hereafter). Among various types of vdW magnets, FGT exhibits relatively high ferromagnetic transition temperature (T_c), large PMA and metallic nature that enables efficient charge/spin transport suitable for spintronic applications^{5,19}. In this study, we

utilize high spatial resolution magnetic imaging techniques, scanning transmission X-ray microscopy (STXM) and Lorentz transmission electron microscopy (LTEM), to directly observe magnetic structures in FGT. We first show the dynamic generation and stabilization of skyrmion crystal (SkX, also referred to as skyrmion lattice) state in FGT, where strong pulse-induced thermal fluctuations transform magnetic domains into SkX. We then examine the stability of SkX against thermal fluctuation and magnetic fields, which eventually constitutes experimental phase diagram of SkX state. Moreover, we demonstrate the static generation of magnetic skyrmions and SkX using a magnetic field applied along an oblique direction. Taking advantage of in-plane magnetization sensitivity in LTEM measurements, we further evidence the homochiral nature of skyrmions stabilized in the SkX state.

Figure 1a schematically shows the crystal structures of monolayered FGT viewed from xy and yz planes and bi-layered FGT exhibiting vdW bonding between monolayers. Each FGT monolayer consists of a Fe_3Ge covalently bonded slab and two Te layers placed above and underneath the Fe_3Ge , and each layer is separated by a 2.95 Å vdW gap in multi-layered stack²⁰. Within a Fe_3Ge slab, two inequivalent Fe sites exist, Fe^{II} (the valence states of Fe^{2+}) and Fe^{III} (the valence states of Fe^{3+}), as indicated in Fig. 1a. Overall, the reduced bulk crystal symmetry in FGT is known to provide a magnetocrystalline anisotropy induced by strong SOC²¹.

For both electrical and transmission microscopy measurements on the same sample, we fabricated Hall-bar type FGT device on a 100-nm-thick Si_3N_4 membrane using soft mechanical exfoliation technique together with e-beam lithography and lift-off [see Methods and Supplementary Information for details]. Figure 1b shows the cross-sectional view of high-resolution transmission electron microscopy (HRTEM) images of the device, where layered high-crystalline quality FGT is observed (Fig. 1b, inset). Note that FGT layer is sandwiched by two

oxidized FGT (O-FGT) due to the sample fabrication under ambient condition, and 5 nm-thick Pt was deposited *ex-situ* as a capping material to prevent further oxidation [see Methods and Supplementary Information for details]. The magnetic hysteresis behaviors of the FGT device were measured using the Hall resistance (R_{xy}) measurement, where external magnetic field was applied to out-of-plane direction at controlled temperatures ranging 100-220 K (Fig. 1c). While the R_{xy} consists of a normal Hall resistance (R_N) and an anomalous Hall resistance (R_{AH}), FGT films exhibit a large value of R_{AH} in R_{xy} , which roughly scales with the magnetization (M_z)⁵. Therefore, the square hysteresis loops at 100 K in Fig. 1c represents an out-of-plane magnetic anisotropy, which persists up to 200 K ($T_C \sim 200$ K). It is noteworthy that R_{xy} measurements yields two distinct slopes (sharp and slanted slopes) in temperature range, $100 \text{ K} \leq T \leq 180 \text{ K}$, and the slanted area becomes more prominent as temperature increases. This area indicates the presence of multi-domain state, where the initially nucleated domains at sharp but incomplete switching propagate across the film, originating from the reduced magnetic anisotropy of FGT at higher temperature due to increased thermal fluctuations. Using this slanted area, we can drive the magnetization into multi-domain state at low temperatures and near zero magnetic fields, as shown in Fig. 1d. Red and blue curves indicate down-to-up and up-to-down switching at 120 K, respectively. For example, at a down-(up-)magnetization saturation state, increasing (decreasing) magnetic field just enough to generate multi-domain states and then subsequently reversing the field drives the overall magnetization into multi-domain states near zero magnetic field. This technique was employed to generate multi-domains during STXM, which require large magnetic moments and multi-domain states for high contrast observations.

Figure 2a shows the schematic of STXM experimental setup, where the temperature of cooling stage was controlled between $100 \text{ K} \leq T \leq 300 \text{ K}$ using liquid nitrogen (LN₂) and heat-

exchanger. The scanning electron microscopy (SEM) image of measured FGT device with Hall-cross geometry and the electrical circuit diagram is also included in Fig. 2a [see Methods for details]. The magnetization state of FGT device was imaged by probing the intensity of transmitted circularly-polarized X-ray at the Fe-edge (L_3 absorption edge), where X-ray magnetic circular dichroism (XMCD) provides contrasts corresponds to the out-of-plane magnetization. Figure 2b shows the magnetic domain configurations in the FGT device as a function of out-of-plane magnetic field, B_z , at 120 K, which confirms strong magnetic contrast observable in FGT from STXM measurements. Note that the alternative field-sweep procedure ($B_z = +200 \text{ mT} \rightarrow -60 \text{ mT} \rightarrow 0 \text{ mT}$) described in Fig. 1d was used to generate the initial magnetic configuration at zero field. The dark and bright contrasts in STXM images correspond to downward ($-M_z$) and upward ($+M_z$) out-of-plane magnetization direction of Fe atoms in FGT, respectively. With increasing out-of-plane field $B_z > 0$, the up domains expand while the down domains shrink into narrow domains, vanishing at the saturation field of $B_z = +80 \text{ mT}$.

Having established that multi-domain states can be readily stabilized and observed in FGT, we then examined the current-induced generation of magnetic skyrmions, as summarized in Fig. 3. In our previous study using conventional chiral ferromagnetic multilayers, Pt/CoFeB/MgO, we demonstrated that the application of bipolar pulses could transform labyrinth domains with chiral domain walls into multiple skyrmions²², and the recent study by Lemesh *et al.* [ref. ²³] unveiled the mechanism to be current-induced thermal transformation into skyrmions, because the energy barrier towards the global skyrmionic ground state decreases with increasing temperature. To utilize the same technique on the FGT device, we applied the burst of 100 bipolar pulses, where the pulse frequency of 1 MHz, the peak-to-peak voltage of $V_{pp} = 2.96 \text{ V}$ and the pulse width of 10 ns were used at $B_z = -40 \text{ mT}$ and 120 K. As shown in Fig. 3a, it is immediate obvious that the

bipolar pulse injection transformed the labyrinth random domain state into multiple circular domain state, where these circular domains turn out to be chiral magnetic skyrmions in Fig. 4. We performed the same procedure at slightly lower temperature, 100 K, and the consistent transformation into multiple skyrmions is observed and the generated skyrmions remain stable at zero magnetic field, $B_z = 0$ mT (highlighted in a blue-boxed area in Fig. 3a). As was observed in ferromagnetic chiral multilayers, the thermal excitation induced by the bipolar pulses may have opened a path towards global skyrmionics state^{22,23}. We examined and observed the consistent domain transformation in another sample capped by graphite, as shown in Supplementary Information. This demonstration with graphite-capping is significant, as it excludes two possible contributions from Pt: i) the spin orbit torques (SOTs) by transmitted spin current caused by the spin-Hall effect (SHE) in Pt²⁴ and ii) the DMI contribution from Pt/O-FGT interface. Further analysis reveals that the average size of zero-field skyrmion is ~ 123 nm at 120 K, and the size decreases down to ~ 80 nm with increased density at 160 K [see Supplementary Information for details].

At such disordered multi-skyrmion state at 100 K, we applied alternative positive and negative magnetic fields with increasing magnitude up to $B_z = \pm 80$ mT with the step of $B_z = \pm 10$ mT, as the application of static fields could annihilate pinned weak skyrmions and rearrange them driven by inter-skyrmion repulsive forces, leading to the stabilization of ordered skyrmion state^{25,26}. Figure 3b shows the zero-field magnetic configuration after the field sweep, and surprisingly, the initial *disordered* magnetic skyrmions transformed into *ordered* hexagonal SkX. The inset of Fig. 3b presents the enlarged STXM images at a magnetic field, $B_z = -80$ mT, where the ordered SkX state is more clearly observable (few SkXs are highlighted with blue colors and white lines for guide). The symmetry of SkX also agrees with the symmetry observed in non-centrosymmetric

B20-type chiral magnets^{9,10}. After stabilizing the SkX state, we then plotted the experimental phase diagram of magnetic configurations in FGT, based on the real-space STXM measurements as summarized in Fig. 3c. We observed three magnetic configuration phases: i) SkX, ii) the co-existence of SkX and multi-domains, and iii) saturated ferromagnetic states, where the representative STXM images of each state are included in the right panel of Fig. 3c. It should be noted that, once generated, SkX in FGT can be stabilized at a wide range of magnetic field and temperature. Moreover, unlike SkX in B20-type chiral magnets^{9,10}, SkX state remains stable at zero magnetic field. Together with the recent discovery of gate-tunable room-temperature magnetization in the same material⁵, it might also be possible to harness and manipulate magnetic skyrmions and their lattice at room temperature and zero magnetic fields, which will constitute a major breakthrough towards room-temperature skyrmion applications based on vdW magnets.

To access the chiral information of observed magnetic configurations, we performed the LTEM measurement as summarized in Fig. 4 [see Methods for details]. Figure 4a shows under-, in-, and over-focused LTEM images of the FGT sample at zero field and 160 K, where magnetic contrasts are only visible in defocused images. It should be noted that the Fresnel-LTEM measurement cannot directly observe Néel-type magnetic configurations at zone-axis mode, due to the cancellation of magnetic inductions between electrons and symmetric in-plane magnetic moments with opposite directions²⁷. Moreover, as shown in the red-boxed areas in the left and right images in Fig. 4a, under- and over-focused LTEM images exhibit the labyrinth domain structures with reserved domain wall contrasts, and such magnetic contrasts agrees with the contrasts observed for Néel-type domain walls in chiral metallic multilayers,^{27,28} implying that the observed SkX state in Fig. 3 may consist of Néel-type chiral skyrmions. Considering that in-plane magnetizations components of Néel-type skyrmions can be further stabilized under the application

of in-plane magnetic fields aligned with the domain walls, we then performed the field cooling (FC) of FGT sample with the magnetic field of $B_z = -40$ mT at an oblique angle, where the sample was tilted about -20° along the x -axis. Figure 4b shows magnetic configurations observed at the tilting angle of -20° (left), 0° (center) and $+20^\circ$ (right) at 160 K. Noticeably, the FC at a tilted magnetic field quasi-statically generated SkX state in FGT crystal, and more importantly, the generated skyrmions are homochiral. We also simulated the LTEM images for Néel-type skyrmion and compared the simulated contrast line profile with experimental observation as shown in Fig. 4c, representing a good agreement [see Methods for simulation details].

With these experimental demonstrations of homochiral skyrmions and their SkX state in FGT, here we discuss the possible source of DMI in vdW FGT crystal. As shown in Fig. 1b, our FGT is relatively thick (~ 60 nm) and symmetrically sandwiched by two O-FGT layers, therefore, asymmetric interface-driven DMI is not expected, thus, the DMI inducing Néel-type magnetic configurations may originate from the FGT crystal itself. To unveil this DMI in FGT, we analyzed possible DMI sources from the FGT crystal symmetry. As discussed earlier, a monolayer of FGT contains three Fe sublayers (i.e., a 2D Fe^{II} and Ge sublayer between two 2D Fe^{III} sublayer), forming a hexagonal structure that is sandwiched between two Te layers. The whole FGT monolayer structure has the non-centrosymmetric point group of $D_{3h}^{20,29}$ and thus in principle, shows no bulk DMI. Indeed, although some locally broken inversion symmetry of sublayers in FGT could result in the DMI that stabilizes Néel-type skyrmions, all possible DMIs in the whole FGT monolayer structure are cancelled with each other as discussed and summarized in Supplementary Information. For example, the top Fe^{III} sublayer and neighboring Te layer forming a lattice of point group of C_{3v} and broken inversion symmetry, where interfacial DMI could be induced at the top Fe^{III} sublayer via the superexchange along the $\text{Fe}^{\text{III}}\text{-Te-Fe}^{\text{III}}$ path, similar to the case of 2D

hexagonal boron nitride structure with buckling³⁰. However, due to the reflection symmetry of the system, the DMIs induced at the top and bottom Fe^{III} sublayers are cancelled with each other and the net DMI in the whole FGT structure vanishes. Although an internal net DMI does not exist in the FGT monolayer structure with the existing theoretical frameworks based on structural symmetry, there still exist possible DMI scenarios in FGT such as the recent report of the DMI that could become an important effect from sample boundaries¹⁷ or asymmetric interface contributions from top and bottom FGT/O-FGT interfaces due to the different interface quality. Nevertheless, further work on a detailed theory of non-vanishing DMI in FGT may be required, and moreover, a further systematic experimental study of the variance of the DMI on FGT thickness or FGT composition could shed light into more precise origin of DMI in FGT shown in this work.

In summary, using high resolution magnetic microscopy, we demonstrated the observation of chiral magnetic skyrmions and their lattice phase stabilization in a vdW ferromagnet FGT. We further examined the stability of SkX in FGT over a wide range of temperature and magnetic field, including its zero-field manifestation. The possibility to achieve magnetic skyrmions and their lattice phase in vdW magnets marks a significant advance in vdW magnet-based spintronics. Along with the large potential of skyrmions for future spintronic devices to store, process, and transmit data with extremely low power cost, this work will foster a new novel route towards 2D magnet-based topological spintronics.

References.

1. Gong, C. *et al.* Discovery of intrinsic ferromagnetism in two-dimensional van der Waals crystals. *Nature* **546**, 265–269 (2017).
2. Huang, B. *et al.* Layer-dependent ferromagnetism in a van der Waals crystal down to the monolayer limit. *Nature* **546**, 270–273 (2017).
3. Song, T. *et al.* Giant tunneling magnetoresistance in spin-filter van der Waals heterostructures. *Science* **360**, 1214–1218 (2018).
4. Klein, D. R. *et al.* Probing magnetism in 2D van der Waals crystalline insulators via electron tunneling. *Science* **360**, 1218–1222 (2018).
5. Deng, Y. *et al.* Gate-tunable room-temperature ferromagnetism in two-dimensional Fe₃GeTe₂. *Nature* **563**, 94 (2018).
6. Burch, K. S., Mandrus, D. & Park, J.-G. Magnetism in two-dimensional van der Waals materials. *Nature* **563**, 47 (2018).
7. Gong, C. & Zhang, X. Two-dimensional magnetic crystals and emergent heterostructure devices. *Science* **363**, eaav4450 (2019).
8. Gibertini, M., Koperski, M., Morpurgo, A. F. & Novoselov, K. S. Magnetic 2D materials and heterostructures. *Nat. Nanotechnol.* **14**, 408 (2019).
9. Mühlbauer, S. *et al.* Skyrmion Lattice in a Chiral Magnet. *Science* **323**, 915–919 (2009).
10. Yu, X. Z. *et al.* Real-space observation of a two-dimensional skyrmion crystal. *Nature* **465**, 901–904 (2010).
11. Dzyaloshinsky, I. A thermodynamic theory of “weak” ferromagnetism of antiferromagnetics. *J. Phys. Chem. Solids* **4**, 241–255 (1958).

12. Moriya, T. Anisotropic Superexchange Interaction and Weak Ferromagnetism. *Phys. Rev.* **120**, 91–98 (1960).
13. Geim, A. K. & Grigorieva, I. V. Van der Waals heterostructures. *Nature* **499**, 419–425 (2013).
14. Novoselov, K. S., Mishchenko, A., Carvalho, A. & Neto, A. H. C. 2D materials and van der Waals heterostructures. *Science* **353**, aac9439 (2016).
15. Mermin, N. D. & Wagner, H. Absence of Ferromagnetism or Antiferromagnetism in One- or Two-Dimensional Isotropic Heisenberg Models. *Phys. Rev. Lett.* **17**, 1133–1136 (1966).
16. Tong, Q., Liu, F., Xiao, J. & Yao, W. Skyrmions in the Moiré of van der Waals 2D Magnets. *Nano Lett.* **18**, 7194–7199 (2018).
17. Hals, K. M. D. & Everschor-Sitte, K. Twists in ferromagnetic monolayers with trigonal prismatic symmetry. *Phys. Rev. B* **99**, 104422 (2019).
18. Behera, A. K., Chowdhury, S. & Das, S. R. Magnetic skyrmions in atomic thin CrI₃ monolayer. *Appl. Phys. Lett.* **114**, 232402 (2019).
19. Fei, Z. *et al.* Two-dimensional itinerant ferromagnetism in atomically thin Fe₃GeTe₂. *Nat. Mater.* **17**, 778 (2018).
20. Deiseroth, H.-J., Aleksandrov, K., Reiner, C., Kienle, L. & Kremer, R. K. Fe₃GeTe₂ and Ni₃GeTe₂ – Two New Layered Transition-Metal Compounds: Crystal Structures, HRTEM Investigations, and Magnetic and Electrical Properties. *Eur. J. Inorg. Chem.* **2006**, 1561–1567 (2006).
21. Zhuang, H. L., Kent, P. R. C. & Hennig, R. G. Strong anisotropy and magnetostriction in the two-dimensional Stoner ferromagnet Fe₃GeTe₂. *Phys. Rev. B* **93**, 134407 (2016).

22. Woo, S. *et al.* Spin-orbit torque-driven skyrmion dynamics revealed by time-resolved X-ray microscopy. *Nat. Commun.* **8**, 15573 (2017).
23. Lemesh, I. *et al.* Current-Induced Skyrmion Generation through Morphological Thermal Transitions in Chiral Ferromagnetic Heterostructures. *Adv. Mater.* **30**, 1805461 (2018).
24. Sinova, J., Valenzuela, S. O., Wunderlich, J., Back, C. H. & Jungwirth, T. Spin Hall effects. *Rev. Mod. Phys.* **87**, 1213–1260 (2015).
25. Nagaosa, N. & Tokura, Y. Topological properties and dynamics of magnetic skyrmions. *Nat. Nanotechnol.* **8**, 899–911 (2013).
26. Woo, S. *et al.* Observation of room-temperature magnetic skyrmions and their current-driven dynamics in ultrathin metallic ferromagnets. *Nat. Mater.* **15**, 501–506 (2016).
27. Jiang, W. *et al.* Mobile Néel skyrmions at room temperature: status and future. *AIP Adv.* **6**, 055602 (2016).
28. Pollard, S. D. *et al.* Observation of stable Néel skyrmions in cobalt/palladium multilayers with Lorentz transmission electron microscopy. *Nat. Commun.* **8**, 14761 (2017).
29. Johansen, Ø., Risinggård, V., Sudbø, A., Linder, J. & Brataas, A. Current Control of Magnetism in Two-Dimensional Fe₃GeTe₂. *Phys. Rev. Lett.* **122**, 217203 (2019).
30. Yu, J.-X., Daly, M. & Zang, J. Thermally driven topology in frustrated systems. *Phys. Rev. B* **99**, 104431 (2019).

Acknowledgments.

S.W. acknowledges the support from IBM Research and the managerial support from Guohan Hu and Daniel Worledge. S.W. also acknowledges Jiadong Zang for reading this manuscript and providing helpful comments. X.Y acknowledges the support from Grants-In-Aid for Scientific Research (A) (Grant No. 19H00660) from Japan Society for the Promotion of Science (JSPS)). T.-E.P., S.J.K., K.M.S., K.K., J.C. and H.C.K. acknowledge the support from the KIST Institutional Program (2E29410) and the National Research Council of Science and Technology (NST) (Grant no. CAP-16-01-KIST) by the Korean government (MSIP). K.K. acknowledges the support from the Basic Research Laboratory Program through the National Research Foundation of Korea (NRF) funded by the MSIT (NRF-2018R1A4A1020696). X.Z. acknowledges the support by the Presidential Postdoctoral Fellowship of The Chinese University of Hong Kong, Shenzhen (CUHKSZ). Y.Z. acknowledges the support by the President's Fund of CUHKSZ, Longgang Key Laboratory of Applied Spintronics, National Natural Science Foundation of China (Grant No. 11574137), and Shenzhen Fundamental Research Fund (Grant Nos. JCYJ20160331164412545 and JCYJ20170410171958839). M.E. acknowledges the support by the Grants-in-Aid for Scientific Research from JSPS KAKENHI (Grant Nos. JP18H03676, JP17K05490 and JP15H05854) and also the support by CREST, JST (Grant Nos. JPMJCR16F1 and JPMJCR1874). X.L. acknowledges the support by the Grants-in-Aid for Scientific Research from JSPS KAKENHI (Grant Nos. 17K19074, 26600041 and 22360122). J.C acknowledges the support of Yonsei-KIST Convergence Research Institute. Y.D.K was supported by Samsung Research & Incubation Funding Center of Samsung Electronics under Project Number SRFC-TB1803-04 and grant from Kyung Hee University in 2018 (No. KHU-20181299). Part of this work was performed at the MAXYMUS endstation at Berlin Electron Storage Ring Society for Synchrotron Radiation II (BESSYII). We thank HZB for the allocation of neutron/synchrotron radiation beamtime. Part of this work was also performed at the PoLLux (X07DA) endstation of the Swiss Light Source, Paul Scherrer Institut (PSI), Villigen, Switzerland. We thank PSI for the allocation of synchrotron radiation beamtime.

Author contributions.

S.W. designed and conceived the study. T.-E.P. prepared films, fabricated devices and performed device characterizations with the support from S.J.K. K.M.S., K.K. and Y.D.K.. T.-E.P, K.M.S., K.K., M.W., S.F., J.R. and S.W. performed STXM experiments at BESSY II in Berlin, Germany and at Swiss Light Source in Villigen, Switzerland. L.P. and X.Y. performed Lorentz-TEM experiments and analyzed the data. X.Z., J.X., Y.Z., M.E. and X.L. provided theoretical analysis on DMI in FGT crystal. T.-E.P. drafted and L.P., X.Z., X.Y. and S.W. revised the manuscript and all authors reviewed the manuscript.

Competing Interests.

The authors declare no competing interests.

Figures.

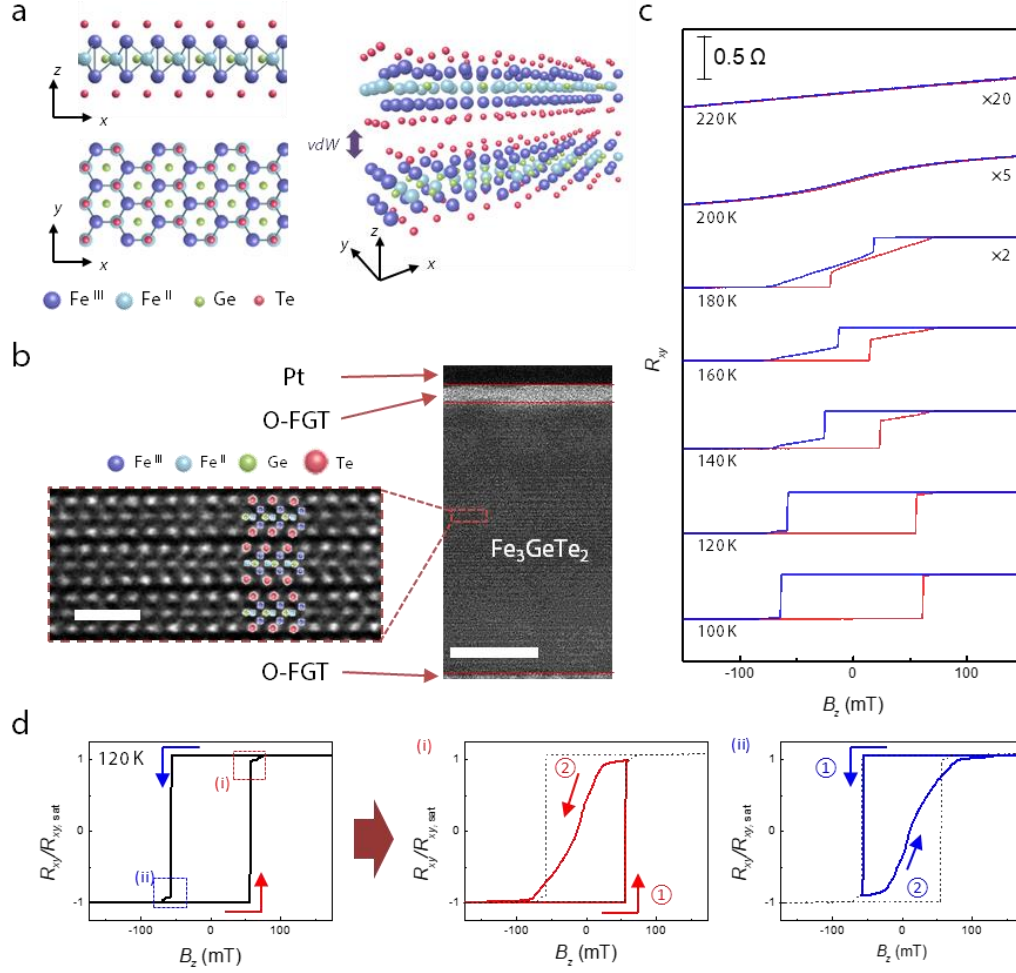


Fig. 1 | Crystal structure and the Hall measurement of a van der Waals Fe_3GeTe_2 . **a**, An atomic structure of a Fe_3GeTe_2 (FGT) mono-layer (left) and the structure of a FGT bi-layer with an interlayer van der Waals (vdW) gap (right). Fe^{III} and Fe^{II} represent the two inequivalent Fe sites in the +3 and +2 vacancy states, respectively. **b**, Cross-sectional high-resolution transmission electron microscopy (HRTEM) image of the FGT with a Pt capping Hall-bar device fabricated on 100 nm -thick Si_3N_4 membrane substrate. (right, scale bar is 20 nm) Oxidized FGT is indicated as O-FGT. The enlarged panel shows the high angle annular dark field (HAADF) image in scanning TEM mode of the red-dashed highlighted area in **b**. (left, scale bar is 2 nm). **c**, Temperature dependent Hall resistance (R_{xy}) as a function of applied out-of-plane magnetic field, B_z . **d**, The measured normalized Hall resistance ($R_{xy}/R_{xy,\text{sat}}$) as a function of magnetic field, B_z , at 120 K , where red and blue dashed rectangular boxes represent the areas of multi-domains in the hysteresis loops (left). Right two hysteresis loops exhibit the magnetic field sequences used for the generation of multi-domains near zero fields from (i) $-B_z$ saturation and (ii) $+B_z$ saturation, respectively. Black dashed lines are included to show the original full saturation hysteresis loops.

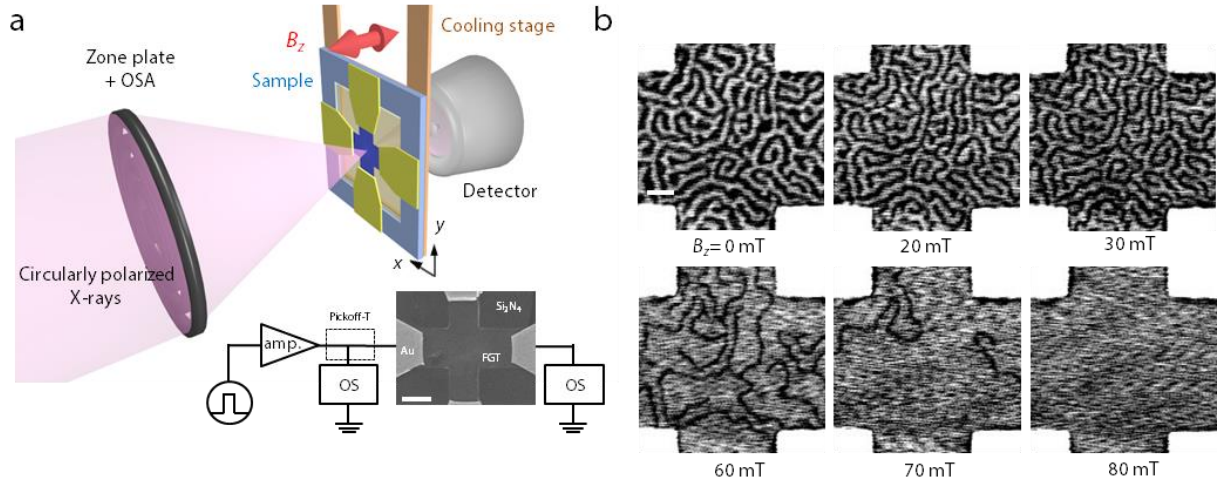


Fig. 2 | Microscopy imaging of domain structures using scanning transmission X-ray microscopy. **a**, Schematic of scanning transmission X-ray microscopy (STXM) experimental setup used for magnetic domain imaging and simultaneous electrical pulse injections. The inset shows scanning electron microscopy (SEM) image of the measured device with Hall bar geometry. Scale bar, 4 μm . Two electrode pads on horizontal x -axis were used for electrical pulse applications, and oscilloscopes before and after device were used to verify the pulse profiles before and after device, respectively. **b**, Exemplary STXM images acquired as a function of increasing magnetic field from $B_z = 0$ mT to $B_z = 80$ mT at 120 K. Dark and bright contrast correspond to magnetization of Fe atoms oriented down ($-M_z$) and up ($+M_z$), respectively. Scale bar, 1 μm .

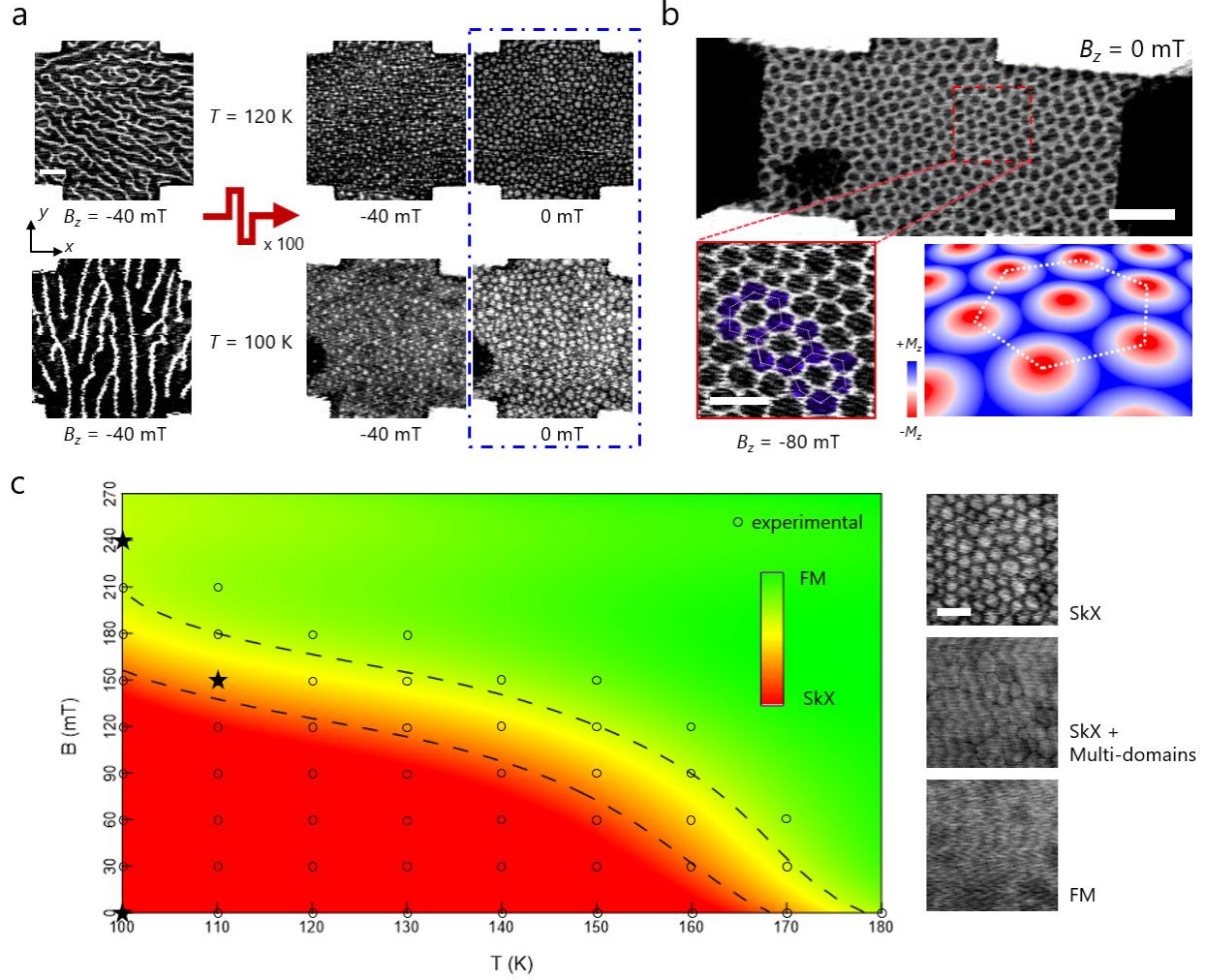


Fig. 3 | Generation and stabilization of magnetic skyrmion lattice phase. **a**, The two images on the left side were acquired at $B_z = -40$ mT at 120 K and 100 K after the initial saturation at $B_z = +200$ mT, respectively, where an initial labyrinth domain states were stabilized. The right two images at $B_z = -40$ mT were acquired after the application of bipolar pulse bursts at 120 K and 100 K, respectively, and the other two images at $B_z = 0$ mT were acquired after removing magnetic fields. Scale bar, 1 μ m. **b**, Representative STXM image of skyrmion crystal (SkX) stabilized over the whole FGT device at $B_z = 0$ mT and $T = 100$ K. Scale bar, 2 μ m. For clarity, the enlarged image of SkX was obtained at $B_z = -80$ mT. Scale bar, 1 μ m. The hexagonal white lines are drawn to guide eye for the ordered SkX, and the inset schematic represents the exemplary magnetic configuration of SkX found in chiral magnets for comparison. Note that skyrmion polarity in **b** ($-M_z$ core) is different from **a** ($+M_z$ core), as the initial field-sweep procedure of reversed field direction was used before the pulse application: $B_z = -200$ mT \rightarrow +40 mT. **c**, Experimental phase diagram of magnetic configurations as a function of temperature and magnetic field. Experimentally measured positions are marked with open circles, and star symbols correspond to exemplary images shown on the right side of the phase diagram. Three representative images show each magnetic configuration state: SkX, SkX + multi-domains, and saturated ferromagnet (FM). Scale bar, 1 μ m. Black dashed lines in phase diagram are guide to the eyes to indicate the phase boundaries.

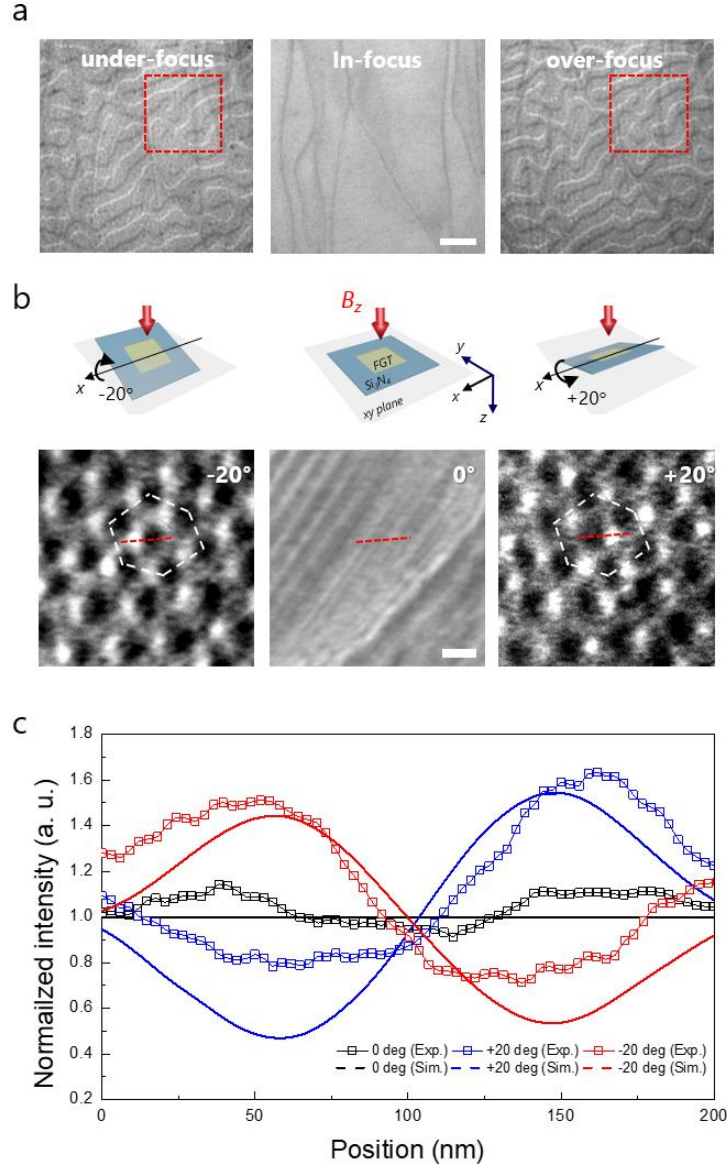


Fig. 4 | Lorentz transmission electron microscopy measurements of skyrmion crystals. **a**, Lorentz transmission electron microscopy (LTEM) images of magnetic configurations at under-focus (left), in-focus (middle) and over-focus (right) acquired at zero field and 160 K, respectively. Scale bar, 500 nm. **b**, LTEM images of magnetic skyrmion crystal (SkX) taken at the sample tilting angle of -20° (left), 0° (middle) and 20° (right) with respect to x -axis at $B_z = -40$ mT and 160 K, respectively. White hexagonal-shaped lines are drawn to guide eye. Scale bar, 200 nm. Schematics indicate the tilted direction of sample. Note that LTEM images in **b** were acquired after field-cooling (FC) of the sample, where the sample was tilted to -20° with respect to x -axis at $B_z = -40$ mT. Solid red lines in **b** were used to acquire contrast profiles. **c**, Experimentally measured (symbols) and simulated (solid lines) contrast profile across a single skyrmion image shown in **b**. Note that the line profile for simulation was acquired by assuming 100 nm-size Néel-type skyrmion.